

Confinement and Kink Entanglement Asymmetry on a Quantum Ising Chain

B. J. J. Khor,^{1,2,*} D.M. Kürkçüoğlu,^{2,3,†} T. J. Hobbs,^{4,‡} G. N. Perdue,^{2,§} and I. Klich^{1,¶}

¹*Department of Physics, University of Virginia, Charlottesville, VA, USA*

²*Fermi National Accelerator Laboratory, Batavia, IL 60510, USA*

³*Superconducting Quantum Materials and Systems Center (SQMS),
Fermi National Accelerator Laboratory, Batavia, IL 60510, USA*

⁴*High Energy Physics Division, Argonne National Laboratory, Argonne, IL 60439, USA*

In this work, we explore the interplay of confinement, string breaking and entanglement asymmetry on a 1D quantum Ising chain. We consider the evolution of an initial domain wall and show that, surprisingly, while the introduction of confinement through a longitudinal field typically suppresses entanglement, it can also serve to increase it beyond a bound set for free particles. Our model can be tuned to conserve the number of domain walls, which gives an opportunity to explore entanglement asymmetry associated with link variables. We study two approaches to deal with the non-locality of the link variables, either directly or following a Kramers-Wannier transformation that maps bond variables (kinks) to site variables (spins). We develop a numerical procedure for computing the asymmetry using tensor network methods and use it to demonstrate the different types of entanglement and entanglement asymmetry.

Strongly-coupled theories such as QCD can possess rich structure-forming properties relevant to many domains in modern physics. Despite advances in nonperturbative methods like lattice gauge theory and phenomenological modeling, a thorough understanding of QCD remains elusive due to the phenomenon of confinement [1]. Recently, entanglement entropy has been suggested as providing a theoretical tool to investigate QCD systems, both in terms of bound states [2–4] and with respect to scattering processes [5–9].

In parallel, quantum spin chains have been proposed as analogous systems to investigate confinement analytically and numerically [10–15]. In particular, the Ising spin chain has been a useful setup to study confinement in real time [16]. Here, a two-fermion system is represented by domain walls, with binding effects introduced via a longitudinal field that gives an energy penalty linearly proportional to the length of the domain wall [17–19]. This configuration simulates key aspects of the confinement of quark-antiquark pairs into mesons, or the binding of two-nucleon systems into the deuteron. This simple model, demonstrating confinement in non-equilibrium quantum quench dynamics, has led to an avalanche of theoretical works [20–34], and the Ising chain confinement was also recently realized on IBM’s quantum hardware [15, 35].

The theory of many-body quantum entanglement can shed insights into confinement and symmetry breaking. Indeed, signatures of confinement show up in entanglement dynamics, where the entanglement entropy is greatly suppressed upon the introduction of the confining field [15, 16, 25]. Symmetry breaking can also manifest in measures of entanglement entropy. When a wave function possesses a local symmetry, its entanglement entropy is a statistical combination of entropies associated to each local occupation

number sector [36–38]. When a local symmetry is broken, however, additional contributions to entropy are generated and can be quantified using “entanglement asymmetry” [39–42]. Various measures of symmetry-resolved entropy have been explored [43–50].

In this Letter, we study the nature of meson dynamics through the lens of entanglement entropy and its asymmetry. In particular, we address the questions: is entropy always suppressed by a confining field? How can one address entanglement asymmetry for a quasi-local conservation law? To do so, we consider the Ising model with transverse and longitudinal fields and an additional three-body term that can be tuned to render the dynamics meson-number conserving for special points in parameter space [51, 52]:

$$H = -J_0 \sum_{i=1}^{L-1} \sigma_i^z \sigma_{i+1}^z - g \sum_{i=2}^{L-1} \sigma_i^x - h \sum_{i=1}^L \sigma_i^z - J \sum_{i=1}^{L-2} \sigma_i^z \sigma_{i+1}^x \sigma_{i+2}^z. \quad (1)$$

This model exhibits confinement in the spreading of meson (kink/anti-kink pair) excitations for nonzero longitudinal fields, $h \neq 0$ [15, 27, 53]. When we set $J = -g$, the model is dual to a fermionic chain coupled with a \mathbb{Z}_2 gauge theory [54]; it is kink-number preserving and exhibits quantum many body scars [51, 52, 55]. When $g \neq -J$, only the kink-number parity is conserved.

We consider the time evolution of an initial domain wall product state of length n , i.e., of the form

$$|j, n\rangle \equiv |\dots \uparrow_j \dots \downarrow_{j+n-1} \uparrow \dots\rangle. \quad (2)$$

Entanglement can be quantified via Rényi entropies,

$$S_n(\rho_A) = \log_2(\text{Tr}(\rho_A^n))/(1-n), \quad (3)$$

where $\rho_A = \text{Tr}_B \rho$ is a reduced density matrix associated with a subset of sites A when its complement, B , has been

integrated out. In particular, the second-order Rényi entropy is $S_2(\rho_A) = -\log_2 \text{Tr}(\rho_A^2)$.

We evaluate $S_2(\rho_A)$ in numerical simulations below. Within time-evolving block decimation (TEBD) [56–58], this generalizes to other entropy orders. Another quantity of interest is the kink density, $\Delta_{i,i+1}^{zz} \equiv \frac{1}{2} \langle (1 - \sigma_i^z \sigma_{i+1}^z) \rangle$, with $\Delta_{i,i+1}^{zz} = 1$ (0) for a spin flip (alignment).

Kink-preserving Dynamics. As mentioned, with the choice $J = -g$, the Hamiltonian in Eq. (1) preserves kink number. To study the evolution of a kink, we project H onto the two-kink subspace in the kink basis, Eq. (2):

$$H_2 = \sum_{\substack{0 \leq j < L-1 \\ 0 < n < L-j-1}} 2hn |j, n\rangle \langle j, n| - (g - J) \left(|j-1, n+1\rangle + |j+1, n-1\rangle + |j, n-1\rangle + |j, n+1\rangle \right) \langle j, n|. \quad (4)$$

This projection is exact when H conserves kink number. We note that the exactness of H_2 offers an opportunity to benchmark tensor network methods against the corresponding computation by exact evolution in the two-kink subspace. In particular, we compare the evolution of the local kink density, as well as the 2nd Rényi entropy as computed by exact diagonalization within the two-kink subspace with corresponding computations within TEBD evolution. Interestingly, we are not aware of any previous calculation of Rényi entropy directly in the two-kink subspace Hamiltonian in Eq. (4), and we outline the computational approach in the supplementary material (SM). We also verify the validity of the two-kink subspace dynamics by comparing the time evolution for various observables and the Rényi entropy with identical quantities computed from small-size exact diagonalization in SM.

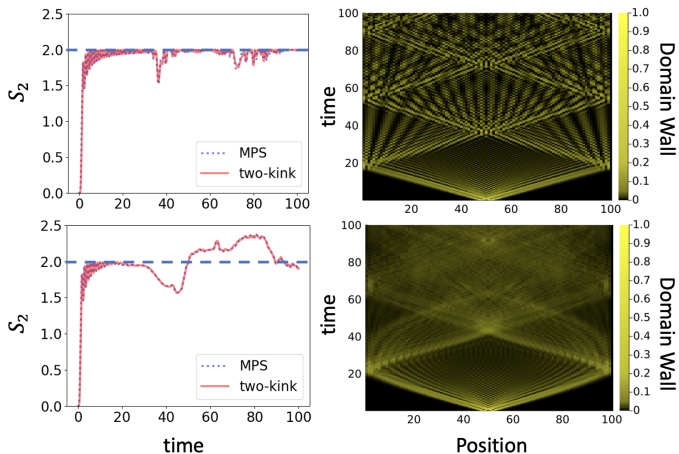


FIG. 1. Evolution of half chain Rényi entropy (left) and domain wall profile (right) following a quench for $g = -J = 0.7$, with (upper) $h = 0$ and (lower) $h = 0.05$.

Rényi Entropy saturation, integrability and confinement. In Fig. 1, we consider the evolution

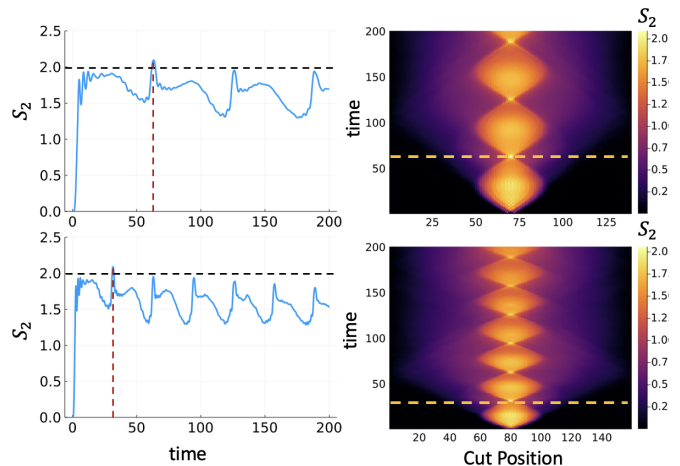


FIG. 2. Half chain $S_2(t)$ (left) and $S_2(t)$ at all cut positions (right) for which the left figure is a slice. Here, $g = -J = 0.25, h = 0.05, L = 140$ (upper) and $g = -J = 0.5, h = 0.1, L = 160$ (lower). See SM for accompanying kink density plot.

of an initially small domain, focusing on the half-chain entropy, $S_2(t)$, and on the kink density. Note the remarkable agreement between the exact diagonalization and TEBD computations, validating the TEBD approach, at least for small kink numbers.

A striking feature of the Rényi entropy dynamics in Fig. 1 (a) is that when $h = 0$, the second-order Rényi entropy saturates at $S_2 \leq 2$. This is surprising at first since a generic two-kink wave function can have a much larger entropy, up to $\log_2(L/2 + 2)$. In the SM, we prove that if $h = 0$, and given an initial two-kink state, we have $S_2 \leq 2$ when kink number is conserved. This bound can be roughly understood as follows: for $h = 0$, Eq. (1) can be mapped to a free-fermion model using a combination of Kramer-Wannier and Jordan-Wigner transformations. With the initial condition of two localized fermions (represented by the kinks) and kink conservation, the subsequent evolution is of two non-interacting fermions, and each fermion can contribute at most $S_2 = \log_2(2) = 1$ due to its delocalization yielding the entropy bound.

The effect of confinement and integrability breaking. What happens when $h > 0$? Naively, one may expect that entropy generation will be decreased, due to the reduction of the spread of the particles.

However, considering Fig. 1 (lower), we encounter a surprise: with a small $h = 0.05$, we find a clear violation of the free-particle ($h = 0$) bound. Indeed, the collisions and interactions with $h \neq 0$ do not correspond to non-interacting particles and are not bound by the above argument. We explore this more closely in Fig. 2. The evolution exhibits the following features: when the string reaches its maximal extent, the entropy starts decreasing, due to a suppression of the wave function spread.

However, close to the minimal string size, where collision is possible, entropy shows a rapid increase. When this collision-related increase is sufficient to overcome suppressed entropy, the $S_2 = 2$ bound is violated. Note that in Fig. 1, the bound violation is enhanced in the presence of a boundary. In Fig. 2 and the accompanying kink density plot in the SM, however, we find that early time collisions can still violate the bound before these boundary effects become substantial, showing that the bound violation may persist also in the thermodynamic limit, $L \rightarrow \infty$. The variations in the Rényi entropy of the system at all cut positions are plotted in the right panels of Fig. 2, showing that the oscillatory behavior of the entropy is reproduced along the internal structure of the meson.

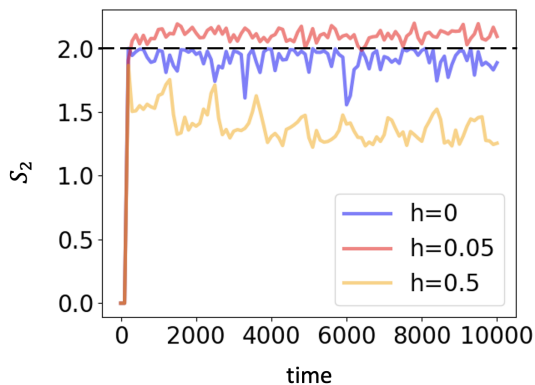


FIG. 3. Long time dynamics of $S_2(t)$ from exact diagonalization of H_2 . Here $g = -J = 0.7$, $L = 100$.

In Fig. 3 we take advantage of the fact that, in exact diagonalization, no Trotterization error is introduced and we can simulate our time evolution dynamics to arbitrarily late times in the exact kink-preserving simulation. Consistent with Fig. 1, when we have $h = 0$, the Rényi entropy is bounded by $S_2 \leq 2$. Upon introducing a small confining field, we see that the Rényi entropy can exceed this upper bound. On the other hand, once the confining field becomes significantly stronger ($h = 0.5$), the Rényi entropy is suppressed compared to the unconfined case, and exhibits oscillatory behavior.

Entanglement Asymmetry. We now turn to our second question. What is the effect of symmetry breaking on entanglement entropy when the symmetry is not exactly local? Given a local symmetry operator of the form $Q = Q_A \otimes I + I \otimes Q_B$ such as charge or magnetization, a useful quantity utilized to study symmetry breaking and its relation to entropy is obtained by projecting ρ_A onto the blocks associated with different symmetry sectors of Q_A :

$$\rho_{A,Q} = \sum_q \Pi_q \rho_A \Pi_q, \quad (5)$$

where Π_q are projectors onto a subspace with a given

eigenvalue q of Q_A . When Q_A has integer eigenvalues, the projected density matrix can be written as

$$\rho_{A,Q} = \int_{-\pi}^{\pi} \frac{d\lambda}{2\pi} e^{-i\lambda Q_A} \rho_A e^{i\lambda Q_A}. \quad (6)$$

This quantity can be used to construct the entanglement asymmetry [39], given by

$$\Delta S_n(\rho_A) = S_n(\rho_{A,Q}) - S_n(\rho_A), \quad (7)$$

where $S_n(\rho_{A,Q}) = \log_2 \text{Tr}(\rho_{A,Q}^n)/(1-n)$ is the symmetry-resolved Rényi entropy. The entanglement asymmetry vanishes, $\Delta S_n = 0$, if computed for a wave function that is an eigenstate of Q .

Kink and Kramers-Wannier Entanglement Asymmetries. In contrast to the discussion above, the conservation of kink number is associated with a quasi-local charge, N_k , since kinks live on the dual lattice, with the number of kinks given by

$$N_k = \sum_{i=1}^{L-1} \Delta_{i,i+1}^{zz} = \frac{1}{2} \left(L - 1 - \sum_{i=1}^{L-1} \langle \sigma_i^z \sigma_{i+1}^z \rangle \right). \quad (8)$$

We break the spin chain into complementary subsystems, A and B , where A contains spins $1, \dots, L_A$; then,

$$N_k = N_{k,A} \otimes I + I \otimes N_{k,B} + \Delta_{L_A, L_A+1}^{zz}, \quad (9)$$

where $N_{k,A}, N_{k,B}$ count the number of kinks within A and its complement B respectively. The last term measures the presence of a kink at the interface between A and B .

The presence of a kink at the interface between A and B is impossible to determine from within A . However, we may compute a coarse-grained entanglement asymmetry by projecting onto blocks with fixed kink number inside A . We define the projected density matrix, $\rho_{A, N_{k,A}}$, as

$$\rho_{A, N_{k,A}} = \int_{-\pi}^{\pi} \frac{d\lambda}{2\pi} e^{-i\lambda N_{k,A}} \rho_A e^{i\lambda N_{k,A}}. \quad (10)$$

This projection is depicted schematically in Fig. 4; from this, we define an asymmetry, $\Delta S_2^{kink} \equiv \Delta S_2(\rho_{A, N_{k,A}})$, as in Eq. (7). We note that asymmetries computed using $\rho_{A, N_{k,A}}$ may be nonzero even if the overall wave function has a fixed kink number. To see this, consider the example of a very simple wave function:

$$\frac{1}{\sqrt{2}} (|\uparrow\uparrow\downarrow\downarrow\rangle + |\uparrow\downarrow\downarrow\uparrow\rangle), \quad (11)$$

where the first two spin sites define subsystem A , giving:

$$\rho_A = \frac{1}{2} (|\uparrow\uparrow\rangle + |\uparrow\downarrow\rangle)(\langle\uparrow\uparrow| + \langle\uparrow\downarrow|). \quad (12)$$

Note that ρ_A describes a pure state with no entropy, however it is *not* in block form from the point of view of internal kinks in subsystem A . On the other hand

$$\rho_{A, N_{k,A}} = \frac{1}{2} (|\uparrow\uparrow\rangle\langle\uparrow\uparrow| + |\uparrow\downarrow\rangle\langle\uparrow\downarrow|) \quad (13)$$

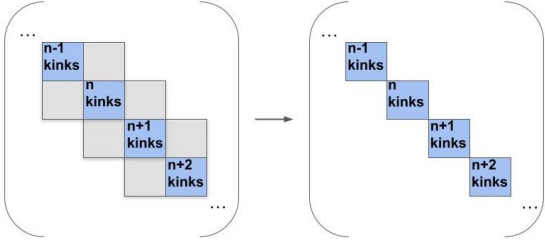


FIG. 4. Left: The reduced density matrix ρ_A for an initial wave function with a fixed number of kinks may have terms coupling n kinks in the bulk of A with $n+1$ or $n-1$ kinks. Right: the projected matrix $\rho_{A, N_k, A}$.

describes a mixed state with entropy $\log_2 2 = 1$. Thus our generalized entanglement asymmetry will only vanish for wave functions that have a fixed number of kinks and no kink at the interface between A and B . The presence of kink at the interface, even with fixed kink number, leads to nonzero asymmetry. Nevertheless, the contribution to the asymmetry, ΔS_2^{kink} , from the boundary kink is small: it will be responsible for at most an $O(1)$ contribution to the entropy, and is thus suitable for probing entropy scaling in large systems.

Next we propose another possible asymmetry measure that vanishes for eigenstates having total kink number N_k . To do so, we use an open boundary Kramers-Wannier (KW) transformation U_{KW} , which maps $|s_1, \dots, s_N\rangle \rightarrow |t_1, \dots, t_N\rangle$ where $t_1 = s_1$ and $t_i = s_{i-1}s_i$ for $i > 1$. In particular, U_{KW} maps kink number into magnetization which is completely local.

Let us consider the relationship between entropies in the original basis vs the KW basis. We take as the set of sites $A = 1, \dots, L_A$ to be fixed. Given a quantum state on the full system we can define $\rho^{KW} = U_{KW}\rho U_{KW}^\dagger$, and $\rho_A^{KW} = \text{Tr}_B \rho^{KW}$. We show in SM that U_{KW} only contains a single two-qubit gate operating between subsystems A, B , and hence $S(\rho_A)$ and $S(\rho_A^{KW})$ differ by at most the entropy that can be generated by such a gate, i.e. at most $2 \log_2 2$. Therefore we can also use $S(\rho_A^{KW})$ for questions of entanglement scaling, i.e., whether entropy is bounded when A is large.

Next, let us discuss entanglement asymmetry related to kink conservation. Note that under U_{KW} , we have $\prod_{i=1}^{l-1} e^{\pm i \lambda \sigma_i^z \sigma_{i+1}^z} \rightarrow \prod_{i=2}^l e^{\pm i \lambda \sigma_i^z}$ (see SM). Thus, following Eqs. (6),(10), we define the KW projected density matrix as:

$$\rho_{N_k, A}^{KW} = \int_{-\pi}^{\pi} \frac{d\lambda}{2\pi} e^{-i\frac{\lambda}{2} \sum_{i=2}^L \sigma_i^z} \rho_A^{KW} e^{i\frac{\lambda}{2} \sum_{i=2}^L \sigma_i^z}, \quad (14)$$

and the KW kink asymmetry as $\Delta S_2^{KW} \equiv S_2(\rho_{N_k, A}^{KW}) - S_2(\rho_A^{KW})$. Note that, ΔS_2^{KW} obeys the desired property: owing to the locality of the kink number operator after the transformation, we have $\Delta S_2^{KW} = 0$ the system is in a state with a fixed number of kinks.

MPS implementation. To proceed beyond the kink conserving dynamics we have developed a Matrix Product State (MPS) procedure to compute S_2 . Given a local charge of interest (magnetization or $N_{k, A}$) we compute the asymmetry by expressing $S_2(\rho_{A, Q})$ as

$$S_2(\rho_{A, Q}) = \int_0^{2\pi} \frac{d\lambda}{\pi} \left(1 - \frac{\lambda}{2\pi}\right) \text{Tr}_A [e^{i\lambda Q_A} \rho_A e^{-i\lambda Q_A} \rho_A]. \quad (15)$$

We carry out the trace in Eq. (15) by representing ρ as a matrix product operator and doing the necessary contractions. A discussion of the complexity of the procedure is provided in SM.

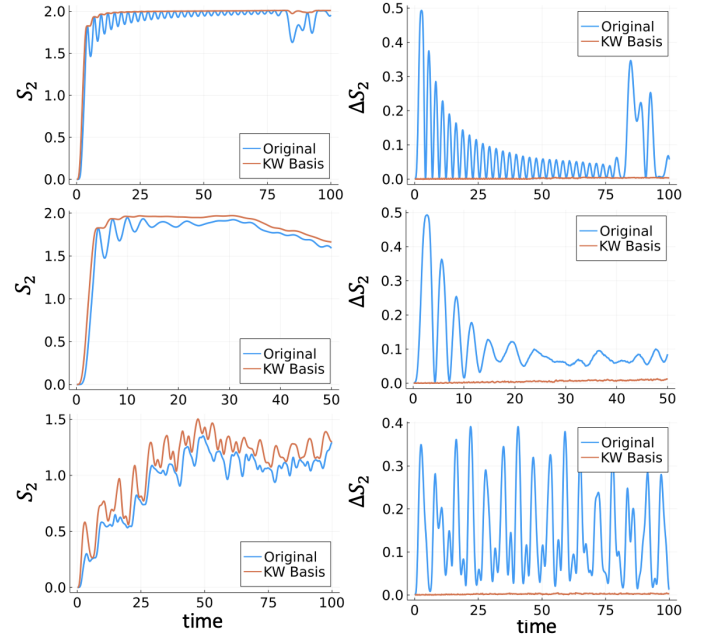


FIG. 5. Entropy and asymmetry for the original basis vs Kramers-Wannier basis. From top to bottom: (Top) $h = 0, L = 100$, (Middle) $h = 0.05, L = 60$, (Bottom) $h = 0.5, L = 100$. The initial state has 4 flipped middle spin $|\uparrow \dots \uparrow \downarrow \downarrow \downarrow \uparrow \dots \uparrow\rangle$. Here, $g = 0.3 = -J$. The evolution is kink number conserving.

Numerical results. We present the numerical results for both the kink-preserving cases and the string breaking cases in Figs. 5 and 6 respectively, in both the original basis and the KW basis, and for Rényi entropy and Rényi asymmetry. We begin by commenting on the cases relating to the kink-preserving case $g = -J$ in Fig. 5. Note that the kink Rényi asymmetry ΔS_2^{kink} does not vanish even when the kink number is conserved, consistent with our example Eq. (11). On the other hand, we verify that ΔS_2^{KW} vanishes, as expected [59].

In Fig. 5, we study three different cases with different confining field strength: (1) the free fermion case $h = 0$, (2) weak confinement, $h = 0.05$, and (3) strong confinement $h = 0.5$. We note that $S_2(\rho_A^{KW})$ and $S_2(\rho_A)$ are quite close to each other. Note that the kink in

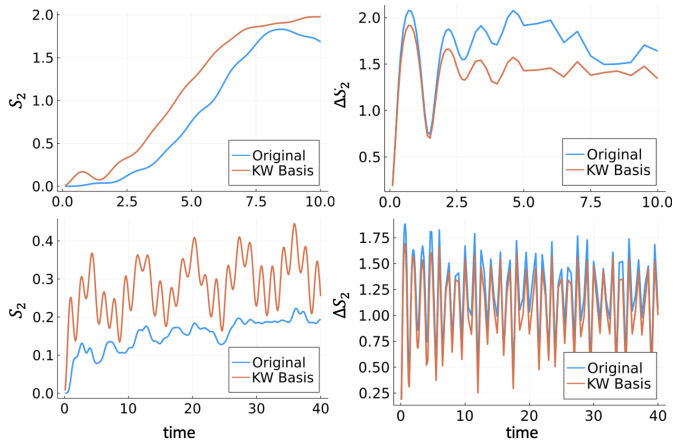


FIG. 6. Entropies and asymmetries in the original vs. the Kramers-Wannier basis. From top to bottom: (Top) $h = 0$, (Bottom) $h = 0.4$. Initial state with 4 flipped middle spins $|\uparrow \dots \uparrow \downarrow \downarrow \downarrow \downarrow \uparrow \dots \uparrow\rangle$. Here $g = 0.4$, $J = 0.1$, $L = 60$. The evolution is not kink conserving.

the strong confining case is oscillating near the entropy cut, which is reflected in the oscillation of the kink asymmetry, while consistent with the construction that KW asymmetry vanishes to a good approximation.

Finally, note that the dip in Rényi entropy around $t \approx 85$ for $h = 0$ in Fig. 5 is associated with collision of kinks, and is accompanied with a spike in kink asymmetry. In general, we observe that dips in S_2 corresponds to spikes in kink asymmetry ΔS_2^{kink} . A kink density heatmap is provided in SM for reference.

Next we consider kink number violating dynamics in Fig. 6. A common feature shared by the Rényi entropy in the kink-preserving Fig. 5 and string breaking Fig. 6 is that the Rényi entropy in the original basis is in general lower than Rényi entropy in the KW basis. This behavior is consistent with the unitary transformation U_{KW} introducing additional entanglement in the system.

On the other hand, the kink entanglement asymmetry ΔS_2^{kink} is greater than the KW kink asymmetry ΔS_2^{KW} , though the difference is more pronounced in the kink-preserving case. This behavior may be attributed to the entropy associated with the possibility of a kink at the center of the chain, exactly at the boundary between the left and right regions.

Conclusion and Outlook. In summary, we studied entanglement associated with meson dynamics via confined string evolution and effects of string breaking; we quantified these phenomena through a novel application of entanglement asymmetry in a QCD-analogue model system, a transverse-field Ising chain with three-spin interaction and longitudinal field. We performed the Rényi entropy calculation directly in the two-kink subspace. For kink-preserving dynamics, the absence of a longitudinal field gives rise to integrability

that sets an upper bound on Rényi entropy. We find that the dynamics of entanglement production generically involves two stages: when the string is contracting, entropy is reduced, followed by an increase when the minimum size is reached. Turning on the confining field can break the integrability bound with weak confining field. However, the Rényi entropy is suppressed upon further increasing the strength of the confining field. This calculation reveals the internal dynamics of a simulated bound-state system resembling the meson in QCD through the lens of entanglement entropy.

Another significant aspect of our work is the study of the interplay of entanglement and kink production in the context of entanglement asymmetry. To do so, we introduced the kink entanglement asymmetry and the Kramers-Wannier entanglement asymmetry to address the nature of kink number in our spin chain. To study these numerically, we devised a new calculation of Rényi asymmetry using MPS methods and demonstrated its application in the context of kink entanglement asymmetry.

We comment on a few future directions that are worthy of consideration. A few recent papers [43, 44, 49] explored and proposed measuring entanglement asymmetry in quantum hardware simulations, and it will be interesting to simulate new types of entanglement asymmetry on NISQ devices. In addition, there is a need to develop a more computationally efficient approach to obtain Rényi asymmetry (see e.g. [60]). Addressing this question might allow us to access later time dynamics for Rényi asymmetry, and to see if dynamical purification [43] can be observed in settings similar to our setup. Finally, lattice gauge theories with site and link variables provide natural playgrounds to explore the concept of kink entanglement asymmetry proposed in this work.

Acknowledgements IK would like to thank German Sierra and Sara Murciano for helpful remarks. B.J.J.K. thanks Joseph Vovrosh for useful discussions about his work. DMK would like to thank Alessandro Roggero for fruitful comments. This document was prepared using the resources of the Fermi National Accelerator Laboratory (Fermilab), a U.S. Department of Energy (DOE), Office of Science, HEP User Facility. Fermilab is managed by Fermi Research Alliance, LLC (FRA), acting under Contract No. DE-AC02-07CH11359. The work of IK was supported in part by the NSF grant DMR-1918207. B.J.J.K., D.M.K., T.J.H., and G.N.P. were partially supported by the DOE HEP QuantISED grant KA2401032. The work of T.J.H. at Argonne National Laboratory was supported by the U.S. Department of Energy under contract DE-AC02-06CH11357. D.M.K. acknowledges partial support by the U.S. Department of Energy, Office of Science, National Quantum Information Science Research Centers, Superconducting Quantum Materials and Systems Center (SQMS) under the contract No.

DE-AC02-07CH11359. The tensor network numerics were implemented using the iTensor package [61, 62].

* bk8wj@virginia.edu

† dogak@fnal.gov

‡ tim@anl.gov

§ perdue@fnal.gov

¶ klich@virginia.edu

- [1] K. G. Wilson, Confinement of quarks, *Phys. Rev. D* **10**, 2445 (1974).
- [2] D. E. Kharzeev and E. M. Levin, Deep inelastic scattering as a probe of entanglement, *Phys. Rev. D* **95**, 114008 (2017), arXiv:1702.03489 [hep-ph].
- [3] H. Lamm, S. Lawrence, and Y. Yamauchi (NuQS), Parton physics on a quantum computer, *Phys. Rev. Res.* **2**, 013272 (2020), arXiv:1908.10439 [hep-lat].
- [4] P. J. Ehlers, Entanglement between valence and sea quarks in hadrons of 1+1 dimensional QCD, *Annals Phys.* **452**, 169290 (2023), arXiv:2209.09867 [hep-ph].
- [5] A. Cervera-Lierta, J. I. Latorre, J. Rojo, and L. Rottoli, Maximal Entanglement in High Energy Physics, *SciPost Phys.* **3**, 036 (2017), arXiv:1703.02989 [hep-th].
- [6] S. R. Beane, D. B. Kaplan, N. Klco, and M. J. Savage, Entanglement Suppression and Emergent Symmetries of Strong Interactions, *Phys. Rev. Lett.* **122**, 102001 (2019), arXiv:1812.03138 [nucl-th].
- [7] Y. Afik and J. R. M. n. de Nova, Entanglement and quantum tomography with top quarks at the LHC, *Eur. Phys. J. Plus* **136**, 907 (2021), arXiv:2003.02280 [quant-ph].
- [8] Q. Liu, I. Low, and T. Mehen, Minimal entanglement and emergent symmetries in low-energy QCD, *Phys. Rev. C* **107**, 025204 (2023), arXiv:2210.12085 [quant-ph].
- [9] M. Carena, I. Low, C. E. M. Wagner, and M.-L. Xiao, Entanglement Suppression, Enhanced Symmetry and a Standard-Model-like Higgs Boson (2023), arXiv:2307.08112 [hep-ph].
- [10] B. M. McCoy and T. T. Wu, Two-dimensional ising field theory in a magnetic field: Breakup of the cut in the two-point function, *Physical Review D* **18**, 1259 (1978).
- [11] G. Delfino, G. Mussardo, and P. Simonetti, Non-integrable quantum field theories as perturbations of certain integrable models, *Nuclear Physics B* **473**, 469 (1996).
- [12] S. Rutkevich, Decay of the metastable phase in $d=1$ and $d=2$ ising models, *Physical Review B* **60**, 14525 (1999).
- [13] M. Bhaeen and A. Tsvelik, Aspects of confinement in low dimensions, *From Fields to Strings: Circumnavigating Theoretical Physics: Ian Kogan Memorial Collection (In 3 Volumes)*, 661 (2005).
- [14] S. Rutkevich, Energy spectrum of bound-spinons in the quantum ising spin-chain ferromagnet, *Journal of Statistical Physics* **131**, 917 (2008).
- [15] J. Vovrosh and J. Knolle, Confinement and entanglement dynamics on a digital quantum computer, *Sci. Rep.* **11**, 11577 (2021), arXiv:2001.03044 [cond-mat.str-el].
- [16] M. Kormos, M. Collura, G. Takács, and P. Calabrese, Real-time confinement following a quantum quench to a non-integrable model, *Nature Physics* **13**, 246 (2017).
- [17] R. Coldea, D. Tennant, E. Wheeler, E. Wawrzynska, D. Prabhakaran, M. Telling, K. Habicht, P. Smeibidl, and K. Kiefer, Quantum criticality in an ising chain: experimental evidence for emergent e8 symmetry, *Science* **327**, 177 (2010).
- [18] Z. Zhang, K. Amelin, X. Wang, H. Zou, J. Yang, U. Nagel, T. Rööm, T. Dey, A. A. Nugroho, T. Lorenz, *et al.*, Observation of e8 particles in an ising chain antiferromagnet, *Physical Review B* **101**, 220411 (2020).
- [19] H. Zou, Y. Cui, X. Wang, Z. Zhang, J. Yang, G. Xu, A. Okutani, M. Hagiwara, M. Matsuda, G. Wang, *et al.*, E8 spectra of quasi-one-dimensional antiferromagnet baco 2 v 2 o 8 under transverse field, *Physical review letters* **127**, 077201 (2021).
- [20] A. J. A. James, R. M. Konik, and N. J. Robinson, Nonthermal states arising from confinement in one and two dimensions, *Phys. Rev. Lett.* **122**, 130603 (2019).
- [21] N. J. Robinson, A. J. James, and R. M. Konik, Signatures of rare states and thermalization in a theory with confinement, *Physical Review B* **99**, 195108 (2019).
- [22] F. Liu, R. Lundgren, P. Titum, G. Pagano, J. Zhang, C. Monroe, and A. V. Gorshkov, Confined quasiparticle dynamics in long-range interacting quantum spin chains, *Phys. Rev. Lett.* **122**, 150601 (2019).
- [23] R. Verdel, F. Liu, S. Whitsitt, A. V. Gorshkov, and M. Heyl, Real-time dynamics of string breaking in quantum spin chains, *Physical Review B* **102**, 014308 (2020).
- [24] R. Verdel, G.-Y. Zhu, and M. Heyl, Dynamical localization transition of string breaking in quantum spin chains, arXiv preprint arXiv:2304.12957 (2023).
- [25] S. Scopa, P. Calabrese, and A. Bastianello, Entanglement dynamics in confining spin chains, *Phys. Rev. B* **105**, 125413 (2022).
- [26] O. A. Castro-Alvaredo, M. Lencsés, I. M. Szécsényi, and J. Viti, Entanglement oscillations near a quantum critical point, *Phys. Rev. Lett.* **124**, 230601 (2020).
- [27] A. Milsted, J. Liu, J. Preskill, and G. Vidal, Collisions of false-vacuum bubble walls in a quantum spin chain, *PRX Quantum* **3**, 020316 (2022).
- [28] P. P. Mazza, G. Perfetto, A. Leroose, M. Collura, and A. Gambassi, Suppression of transport in nondisordered quantum spin chains due to confined excitations, *Phys. Rev. B* **99**, 180302 (2019).
- [29] A. Bastianello, U. Borla, and S. Moroz, Fragmentation and emergent integrable transport in the weakly tilted ising chain, *Phys. Rev. Lett.* **128**, 196601 (2022).
- [30] A. Leroose, F. M. Surace, P. P. Mazza, G. Perfetto, M. Collura, and A. Gambassi, Quasilocalized dynamics from confinement of quantum excitations, *Phys. Rev. B* **102**, 041118 (2020).
- [31] P. I. Karpov, G.-Y. Zhu, M. P. Heller, and M. Heyl, Spatiotemporal dynamics of particle collisions in quantum spin chains, *Phys. Rev. Res.* **4**, L032001 (2022).
- [32] O. Pomponio, M. A. Werner, G. Zarand, and G. Takacs, Bloch oscillations and the lack of the decay of the false vacuum in a one-dimensional quantum spin chain, *SciPost Phys.* **12**, 061 (2022).
- [33] G. Lagnese, F. M. Surace, M. Kormos, and P. Calabrese, False vacuum decay in quantum spin chains, *Phys. Rev. B* **104**, L201106 (2021).
- [34] G. Lagnese, F. M. Surace, S. Morampudi, and F. Wilczek, Detecting a long lived false vacuum with quantum quenches, arXiv preprint arXiv:2308.08340 (2023).
- [35] A. Sopena, M. H. Gordon, G. Sierra, and E. López,

- Simulating quench dynamics on a digital quantum computer with data-driven error mitigation, *Quantum Science and Technology* **6**, 045003 (2021).
- [36] I. Klich and L. Levitov, Scaling of entanglement entropy and superselection rules, arXiv preprint arXiv:0812.0006 (2008).
- [37] D. Dasenbrook and C. Flindt, Dynamical generation and detection of entanglement in neutral leviton pairs, *Physical Review B* **92**, 161412 (2015).
- [38] H. Barghathi, C. Herdman, and A. Del Maestro, Rényi generalization of the accessible entanglement entropy, *Physical Review Letters* **121**, 150501 (2018).
- [39] F. Ares, S. Murciano, and P. Calabrese, Entanglement asymmetry as a probe of symmetry breaking, *Nature Communications* **14**, 2036 (2023).
- [40] F. Ares, S. Murciano, E. Vernier, and P. Calabrese, Lack of symmetry restoration after a quantum quench: An entanglement asymmetry study, *SciPost Phys.* **15**, 089 (2023).
- [41] F. Ferro, F. Ares, and P. Calabrese, Non-equilibrium entanglement asymmetry for discrete groups: the example of the xy spin chain (2023), arXiv:2307.06902 [cond-mat.stat-mech].
- [42] L. Capizzi and M. Mazzoni, Entanglement asymmetry in the ordered phase of many-body systems: the ising field theory (2023), arXiv:2307.12127 [cond-mat.stat-mech].
- [43] V. Vitale, A. Elben, R. Kueng, A. Neven, J. Carrasco, B. Kraus, P. Zoller, P. Calabrese, B. Vermersch, and M. Dalmonte, Symmetry-resolved dynamical purification in synthetic quantum matter, *SciPost Phys.* **12**, 106 (2022).
- [44] A. Rath, V. Vitale, S. Murciano, M. Votto, J. Dubail, R. Kueng, C. Branciard, P. Calabrese, and B. Vermersch, Entanglement barrier and its symmetry resolution: Theory and experimental observation, *PRX Quantum* **4**, 010318 (2023).
- [45] M. Goldstein and E. Sela, Symmetry-resolved entanglement in many-body systems, *Phys. Rev. Lett.* **120**, 200602 (2018).
- [46] S. Murciano, P. Calabrese, and L. Piroli, Symmetry-resolved page curves, *Phys. Rev. D* **106**, 046015 (2022).
- [47] S. Murciano, G. Di Giulio, and P. Calabrese, Entanglement and symmetry resolution in two dimensional free quantum field theories, *Journal of High Energy Physics* **2020**, 73 (2020).
- [48] R. Bonsignori, P. Ruggiero, and P. Calabrese, Symmetry resolved entanglement in free fermionic systems, *Journal of Physics A: Mathematical and Theoretical* **52**, 475302 (2019).
- [49] A. Neven, J. Carrasco, V. Vitale, C. Kokail, A. Elben, M. Dalmonte, P. Calabrese, P. Zoller, B. Vermersch, R. Kueng, and B. Kraus, Symmetry-resolved entanglement detection using partial transpose moments, *npj Quantum Information* **7**, 152 (2021).
- [50] S. Murciano, F. Ares, I. Klich, and P. Calabrese, Entanglement asymmetry and quantum mpemba effect in the xy spin chain, arXiv preprint arXiv:2310.07513 (2023).
- [51] Z.-Y. Ge, Y.-R. Zhang, and F. Nori, Meson instability of quantum many-body scars in a 1d lattice gauge theory (2023), arXiv:2303.13156 [cond-mat.str-el].
- [52] T. Iadecola and M. Schecter, Quantum many-body scar states with emergent kinetic constraints and finite-entanglement revivals, *Phys. Rev. B* **101**, 024306 (2020).
- [53] J. Vovrosh, R. Mukherjee, A. Bastianello, and J. Knolle, Dynamical hadron formation in long-range interacting quantum spin chains, *PRX Quantum* **3**, 040309 (2022).
- [54] U. Borla, R. Verresen, F. Grusdt, and S. Moroz, Confined phases of one-dimensional spinless fermions coupled to Z_2 gauge theory, *Phys. Rev. Lett.* **124**, 120503 (2020).
- [55] E. J. Gustafson, A. C. Y. Li, A. Khan, J. Kim, D. M. Kurkcuoglu, M. S. Alam, P. P. Orth, A. Rahmani, and T. Iadecola, Preparing quantum many-body scar states on quantum computers, *Quantum* **7**, 1171 (2023).
- [56] S. R. White and A. E. Feiguin, Real-time evolution using the density matrix renormalization group, *Phys. Rev. Lett.* **93**, 076401 (2004).
- [57] G. Vidal, Efficient simulation of one-dimensional quantum many-body systems, *Phys. Rev. Lett.* **93**, 040502 (2004).
- [58] F. Verstraete, J. J. García-Ripoll, and J. I. Cirac, Matrix product density operators: Simulation of finite-temperature and dissipative systems, *Phys. Rev. Lett.* **93**, 207204 (2004).
- [59] Due to the approximate nature of the TEBD time evolution on the MPS, we note that there is error of order 10^{-3} on the kink number conservation, and the magnetization asymmetry error is fluctuating in order of 10^{-3} .
- [60] N. Feldman, A. Kshetrimayum, J. Eisert, and M. Goldstein, Entanglement estimation in tensor network states via sampling, *PRX Quantum* **3**, 030312 (2022).
- [61] M. Fishman, S. R. White, and E. M. Stoudenmire, The ITensor Software Library for Tensor Network Calculations, *SciPost Phys. Codebases* , 4 (2022).
- [62] M. Fishman, S. R. White, and E. M. Stoudenmire, Codebase release 0.3 for ITensor, *SciPost Phys. Codebases* , 4 (2022).
- [63] B. Bertini, K. Klobas, M. Collura, P. Calabrese, and C. Rylands, Dynamics of charge fluctuations from asymmetric initial states (2023), arXiv:2306.12404 [cond-mat.stat-mech].
- [64] L. Capizzi and V. Vitale, A universal formula for the entanglement asymmetry of matrix product states (2023), arXiv:2310.01962 [quant-ph].
- [65] M. Ostmann, M. Marcuzzi, J. P. Garrahan, and I. Lesanovsky, Localization in spin chains with facilitation constraints and disordered interactions, *Phys. Rev. A* **99**, 060101 (2019).
- [66] M. A. Nielsen and I. L. Chuang, *Quantum Computation and Quantum Information: 10th Anniversary Edition* (Cambridge University Press, 2011).

Appendix A: Benchmarking exact diagonalization, two-kink dynamics and tensor network simulations

In this appendix, we present numerical data benchmarking. (1) We study the time evolution dynamics of the spin, initial domain wall, and Rényi entropy for both the exact diagonalization and the two-kink Hamiltonian dynamics, both at the special point $J = -g$ (where they should match) and $J \neq -g$ (where they generally differ). (2) We compare the time evolution dynamics for the initial domain wall and Rényi entropy for tensor network simulation and two-kink dynamics for larger system size.

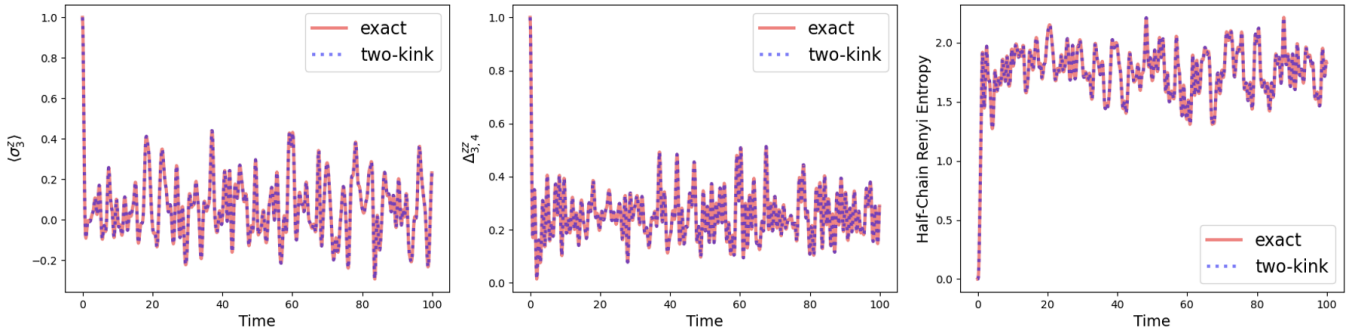


FIG. 7. From left to right: The spin expectation value $\langle \sigma_3^z \rangle$, the domain wall expectation value $\Delta_{3,4}^{zz}$ and the half chain Rényi entropy S_2 at parameter values $g = 0.7 = -J, h = 0.1$ for both exact and two-kink dynamics. At this special point where $g = -J$, the time evolution dynamics for the exact diagonalization can be described exactly by two-kink subspace dynamics.

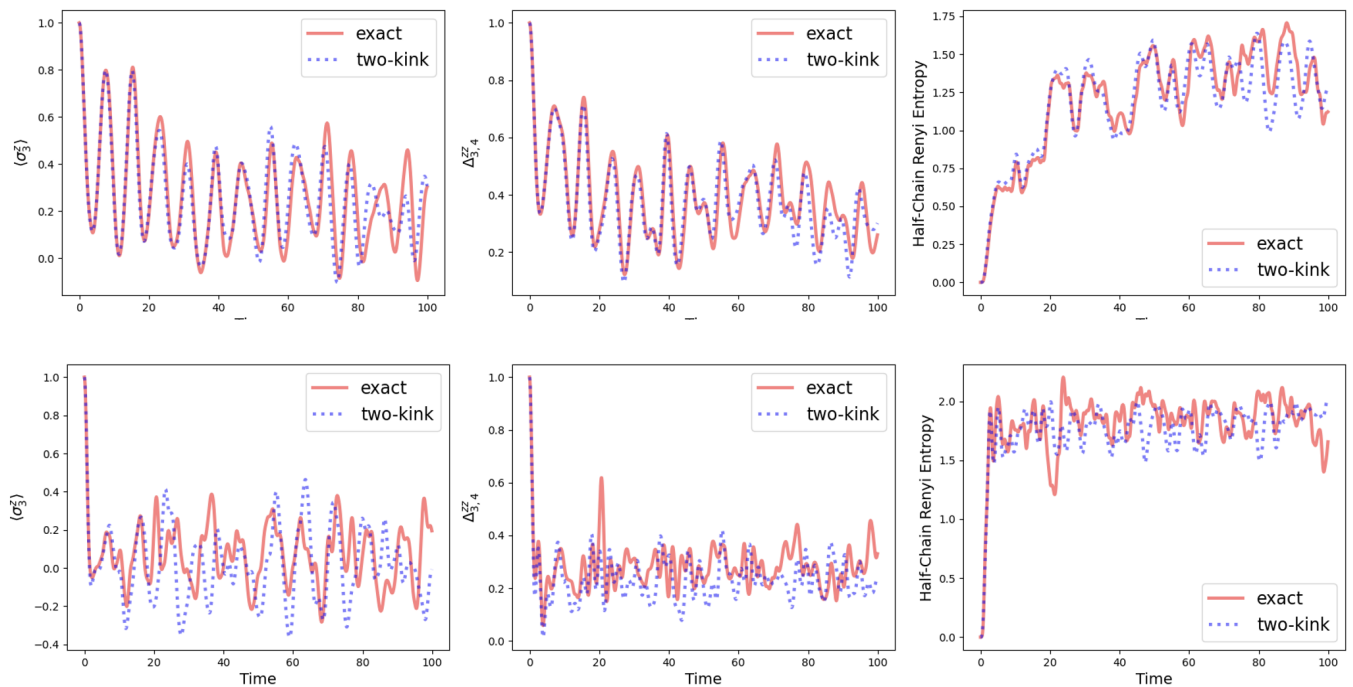


FIG. 8. From left to right: The spin expectation value $\langle \sigma_3^z \rangle$, the domain wall expectation value $\Delta_{3,4}^{zz}$ and the half chain Rényi entropy S_2 . From top to bottom: The set of physical quantities at the top panel was simulated at $g = 0.3, h = 0.4$ and $J = -0.05$ while the bottom panel was at $g = 0.6, h = 0.1, J = -0.1$. Note that the top panel corresponds to a more confined dynamics, where the deviation of the time evolution and exact diagonalization occurs only at late time, while for parameter with less confinement (smaller h), the deviation is significant even at early times.

For the first benchmarking between exact diagonalization and two-kink dynamics (to establish the reliability of two-kink dynamics in kink-conserving cases), we initialize the quantum state of a $L = 10$ quantum Ising spin chain to $|\psi_0\rangle = |\uparrow\uparrow\uparrow\uparrow\downarrow\downarrow\uparrow\uparrow\uparrow\rangle$, and time evolve the state using (a) exact diagonalization of the Hamiltonian in Eq. 1

and (b) two-kink Hamiltonian in Eq. 4. For Fig. 7 and 8, the spin expectation values $\langle \sigma_i^z(t) \rangle$ are tracked at the underlined spin $|\uparrow\uparrow\uparrow\uparrow\downarrow\downarrow\uparrow\uparrow\uparrow\rangle$ in the initial state $|\psi_0\rangle$, and the domain wall expectation values $\Delta_{i,i+1}^{zz}(t)$ are tracked at $|\uparrow\uparrow\uparrow\uparrow\downarrow\downarrow\uparrow\uparrow\uparrow\rangle$, and the Rényi entropy is cut at half chain bipartition respectively.

In Fig. 7, we see that the time evolution of the various different physical quantities of interest match between exact diagonalization and two-kink subspace evolution. As demanded by the symmetry of the Hamiltonian when $g = -J$, the domain wall number at this special line is exactly conserved.

We then turn to the string breaking (more generic) cases, where kink number is not conserved. In Fig. 8, we observe that while we generally expect the dynamics of the exact Hamiltonian to differ from that from the two-kink subspace projection at $g \neq -J$, the macroscopic expectation values for spin $\langle \sigma_i^z \rangle$ and domain wall $\Delta_{i,i+1}^{zz}$ overlaps significantly for early times and only deviate at later time for strong confining field h . In contrast, with weak confining field h the dynamics deviates significantly at early times. This establishes the general physics and intuition that with strong confinement h , two-kink approximation is reasonable for quantum quench problem with initial state $|\uparrow \dots \uparrow \downarrow \dots \downarrow \uparrow \dots \uparrow\rangle$.

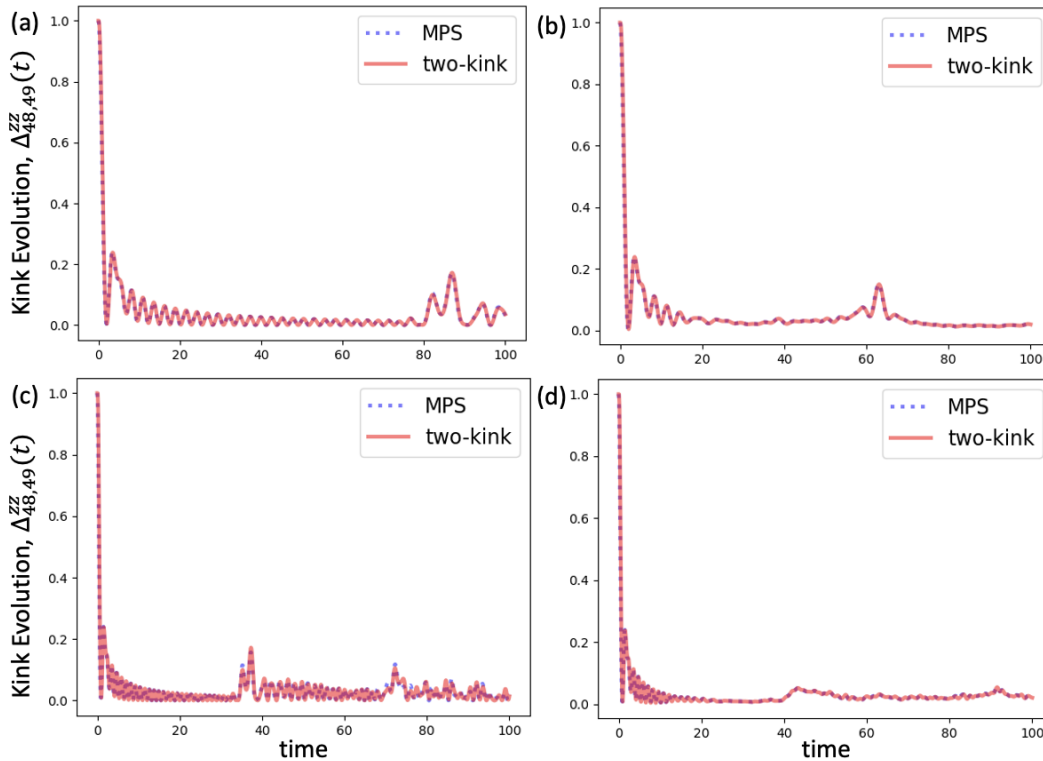


FIG. 9. The set of parameter values used for the time evolution of the domain wall $\Delta_{48,49}^{zz}$ at position 48 and 49 following a quantum quench are (a) $g = 0.3, J = -0.3, h = 0$, (b) $g = 0.3, J = -0.3, h = 0.05$, (c) $g = 0.7, J = -0.7, h = 0.0$, (d) $g = 0.7, J = -0.7, h = 0.05$.

After verifying the validity of the two-kink dynamics for kink-conserving dynamics, we then turn to the benchmarking of the tensor network simulations with the two-kink dynamics. In the main article, we provided the benchmarking of MPS with two-kink dynamics for the time evolution of the Rényi entropy S_2 for $g = -J = 0.7$ in Fig. 1. Here, we provide additional numerical simulations of the domain wall profile located at the initial domain wall positions at 48th and 49th sites for a spin chain of length $L = 100$ and initial state with 4 middle flipped spin $|\uparrow_1 \dots \uparrow_{48} \downarrow_{49} \downarrow_{50} \downarrow_{51} \downarrow_{52} \uparrow_{53} \dots \uparrow_{100}\rangle$, as shown in Fig. 9. This provides an additional check (besides the Rényi entropy dynamics) that the MPS time evolution from TEBD is approximated well by two-kink time evolution.

Appendix B: Construction of the reduced density matrix in the Two-Kink Subspace

In this section, we outline the overall approach we used to construct the reduced density matrix in the two-kink subspace in order to calculate the 2nd order Rényi entropy for dynamics within the two-kink subspace. We represent

all possible two-kink states in a spin chain of length L , $|\uparrow_1 \dots \uparrow_{j_L-1} \downarrow_{j_L} \dots \downarrow_{j_R} \uparrow_{j_R+1} \dots \uparrow_L\rangle$, with the two number representation $|j_L, j_R\rangle$, where j_L is the position of the left domain wall and j_R is the position of the right domain wall. In the two-kink Hilbert space, for sites $i = 1, \dots, L$, the two numbers can take the following values $1 < j_L \leq j_R < L$.

With this two-number representation, a quantum spin chain of size L will have a two-kink subspace of dimension $(L-1)(L-2)/2$. To proceed with the Rényi entropy calculation, given a bipartition bond l_B separating the spin chain into left-right bipartition with sites $1, \dots, l_B$ to the left side of the chain and sites $l_B + 1, \dots, L$ to the right, we will proceed to perform bipartition in the two-kink states

$$\begin{aligned}
|\psi\rangle = & \sum_{1 < j_L \leq j_R \leq l_B < L} \alpha_{j_L, j_R} |\text{one/two-kink}\rangle_L |\text{no-kink}\rangle_R + \sum_{1 < j_L \leq l_B < j_R < L} \alpha_{j_L, j_R} |\text{one-kink}\rangle_L |\text{one-kink}\rangle_R \\
& + \sum_{1 \leq l_B < j_L \leq j_R < L} \alpha_{j_L, j_R} |\text{no-kink}\rangle_L |\text{one/two-kink}\rangle_R, \tag{B1}
\end{aligned}$$

where we decompose the sum into three types of terms classified by the location of the bipartition cut relative to the domain wall positions. Here, the states with label $|\text{one-kink}\rangle_L |\text{no-kink}\rangle_R$ and $|\text{no-kink}\rangle_L |\text{one-kink}\rangle_R$ are cases where the bipartition cut l_B coincides with one of the left/right domain walls.

Constructing the full pure state density matrix $|\psi\rangle\langle\psi|$ and taking the partial trace over the right partition, we have

$$\begin{aligned}
\rho_L = \text{Tr}_R(|\psi\rangle\langle\psi|) = & \sum_{1 < j_L \leq j_R \leq l_B} \sum_{1 < j'_L \leq j'_R \leq l_B} \alpha_{j_L, j_R} \alpha_{j'_L, j'_R}^* |\text{one/two-kink}\rangle\langle\text{one/two-kink}| \\
& + \sum_{1 < j_L \leq l_B} \sum_{1 < j'_L \leq l_B} \left(\sum_{l_B < j_R < L} \alpha_{j_L, j_R} \alpha_{j'_L, j'_R}^* \right) |\text{one-kink}\rangle\langle\text{one-kink}| \\
& + \left(\sum_{l_B < j_L \leq j_R < L} \alpha_{j_L, j_R} \alpha_{j_L, j_R}^* \right) |\text{no-kink}\rangle\langle\text{no-kink}| \\
& + \sum_{1 < j_L \leq l_B} \left(\sum_{l_B < j_R < L} \alpha_{j_L, j_R} \alpha_{j'_L = l_B + 1, j_R}^* \right) |\text{one-kink}\rangle\langle\text{no-kink}| \\
& + \sum_{1 < j'_L \leq l_B} \left(\sum_{l_B < j_R < L} \alpha_{j'_L, j_R}^* \alpha_{j_L = l_B + 1, j_R} \right) |\text{no-kink}\rangle\langle\text{one-kink}| \tag{B2}
\end{aligned}$$

We shall elaborate on each term below.

The first term

The first term in Eq. (B2) is obtained from the multiplying the first terms of Eq. (B1) in both $|\psi\rangle$ and $\langle\psi|$, followed by partial right trace over all spin-up state $|\text{no-kink}\rangle_R$. Hence, the coefficients in the first term in Eq. (B2) can be understood to be constructed without performing any sum from partial tracing.

The second term

The second term in Eq. (B2) is obtained by multiplying the second terms of Eq. (B1) in both $|\psi\rangle$ and $\langle\psi|$, followed by partial right trace over $|\text{one-kink}\rangle_R$. In this case, the coefficients in the second term in Eq. (B2) is constructed from summing over $l_B < j_R = j'_R < L$ where the right partition states $|\text{one-kink}\rangle$ and $\langle\text{one-kink}|$ must agree in the partial trace process.

We also note here that terms labelled as 'the second term' is actually a subset of 'the first term' and not a new set of distinct terms (which we label separately only because they had different origin), so the coefficients here should add to the coefficients of the first term when the states are the same.

The third term

The third term in Eq. (B2) is actually a single state, and its coefficient is constructed from a sum over the modulo square $|\alpha_{j_L, j_R}|^2$ for $l_B < j_L \leq j_R < L$. Here j_L and j_R both lie on the right partition basis states, for which the indices must match (hence mod square) when one performs the partial trace.

The fourth and fifth terms

The fourth and the fifth term in Eq. (B2) are the complex conjugate of each other, so it suffices to explain one of them. The fourth term comes from the cross multiplication of the second term $|\text{one-kink}\rangle|\text{one-kink}\rangle$ and the third term of type $\langle \text{no-kink} | \langle \text{one-kink} |$ in Eq. (B1).

Note that the third term of the form $\langle \text{no-kink} | \langle \text{two-kink} |$ cannot contribute since the right partition partial cannot match those from $|\text{one-kink}\rangle|\text{one-kink}\rangle$. This explains the setting of $j'_L = l_B + 1$ in the coefficient of the fourth term (likewise the corresponding term in the fifth term). We also understand that there is a single sum matching the indices $j_R = j'_R$ over the range $l_B < j_R < L$ when one constructs the coefficients of the fourth and the fifth term.

Matrix representation of the reduced density matrix

Collecting these terms, it helps to visualize these various terms on a matrix representation. We label row sectors according to $|\text{two-kink}\rangle$, $|\text{one-kink}\rangle$ and $|\text{no-kink}\rangle$ and likewise for the column sectors. The matrix representation is as below.

$$\rho_L = \begin{pmatrix} \begin{array}{c|c|c} \text{First term} & \text{First term} & 0 \\ \hline |\text{two-kink}\rangle\langle \text{two-kink}| & |\text{two-kink}\rangle\langle \text{one-kink}| & \\ \hline \text{First term} & \text{First + Second term} & \text{Fourth term} \\ |\text{one-kink}\rangle\langle \text{two-kink}| & |\text{one-kink}\rangle\langle \text{one-kink}| & |\text{one-kink}\rangle\langle \text{no-kink}| \\ \hline 0 & \text{Fifth term} & \text{Third term} \\ & |\text{no-kink}\rangle\langle \text{one-kink}| & |\text{no-kink}\rangle\langle \text{no-kink}| \end{array} \end{pmatrix}$$

Here, the third row is a single row and the third column is a single column. The reduced density matrix can then be used to calculate the Rényi entropy for the two-kink dynamics.

Appendix C: Rényi Entropy Evolution and Collisions: Early time and Entropy bound violation with large system size

In this appendix, we cover two points. (1) We outline several qualitative features of the Rényi entropy evolution that highlight several interesting features that are not discussed in the main article. (2) In addition, we show that the entropy bound violation with confining field is independent of the finite system size effect. We will mainly concern ourselves with the kink-preserving dynamics in this appendix.

For generic model parameters, as the initial product state domain wall starts evolving, entanglement immediately appears, dominated by the dynamics of kink-anti kink pair creation and motion. In contrast, for kink-number preserving dynamics, the half-chain entanglement can only begin emerging when the kinks collide. To see this, we compute the Rényi entropy of half of the chain. In Fig. 10, we show how a rapid increase in the half-chain Rényi entropy S_2 for small domain wall and large domain wall separation is associated to the time of the domain wall spreading and collision. Here, a small initial domain wall separation ($l = 4$) has a collision around $t \approx 1$ while that of the large separation $l = 24$ has collision around $t \approx 5$.

We provide additional details for the Rényi entropy dips found in Fig. 5. Here, the dip around $t \approx 85$ is directly associated with kink collision after bouncing off the open boundary chain. We provide the associated domain wall/kink heatmap in Fig. 11.

We now turn to demonstrate that the violation of the $S_2 = 2$ bound is independent of the system size, along with other qualitative features of the entropy evolution. In Fig. 12, we vary various parameters within the kink-conserving dynamics: (1) the kinetic energy ($g - J$), (2) the confining potential field h , and (3) the system size L .

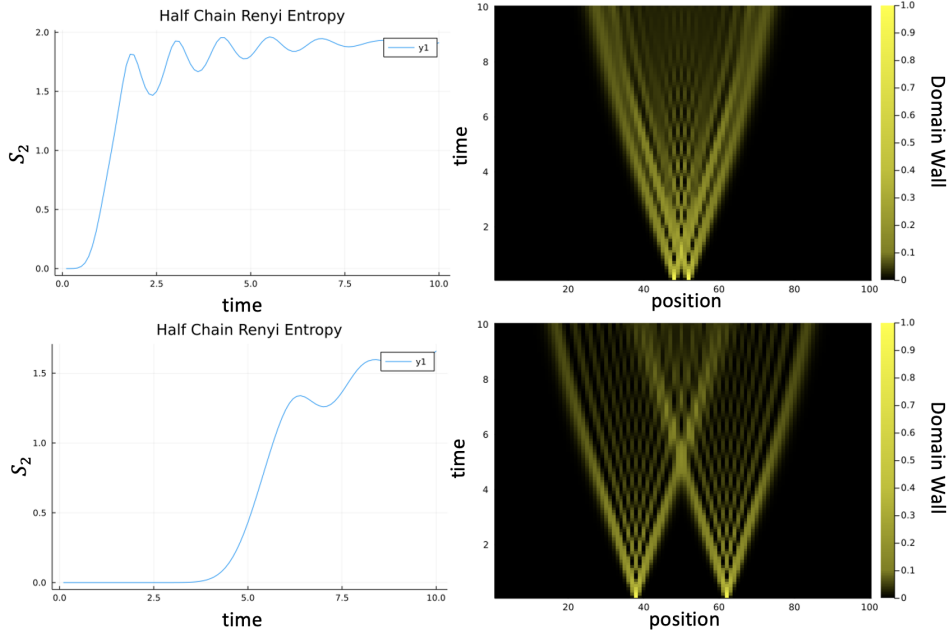


FIG. 10. The half-chain Rényi entropy S_2 (left) and the domain wall profile across link positions (right) for the parameter value set $g = -J = 0.7, h = 0.1$. Here the top diagrams are results from initial state with domain wall separation $l = 4$ (4 down spins in the middle) while the bottom diagrams are results with initial domain wall separation $l = 24$. The increase in S_2 in the early time roughly coincides with the time scale of collision for kink-conserving dynamics.

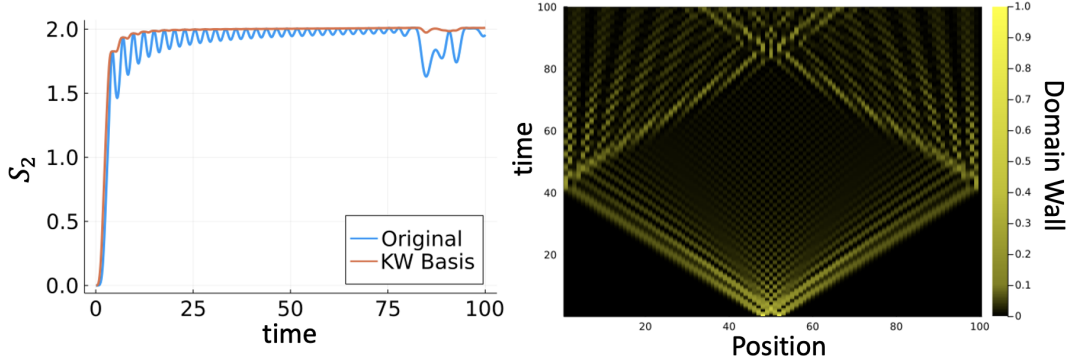


FIG. 11. The half-chain Rényi entropy S_2 (left) and domain wall heat (right) for $g = -J = 0.3, h = 0, L = 100$, and initial domain wall separation size $l = 4$. The dip around $t \approx 85$ corresponds to kink collisions. The color scale has been magnified near $\Delta_{i,i+1}^{zz} = 0$ as the kink density becomes diluted upon spreading.

In Fig. 12, we see the S_2 entropy bound is violated upon the second collision of the kinks. The first collision happens at early time and is discussed in detail earlier in this appendix. Here, we verify that the total kink density near the ends of the chain is negligible when the second collision occurs upon the acceleration of the kink dynamics back to the middle of the chain owing to the confining potential.

Another feature of the kink-conserving dynamics is the dip in the Rényi entropy before the periodic collisions of the kinks after expanding to maximal extent set by the strength of the confining potential. This can be observed in the half-chain Rényi entropy, as well as in the Rényi entropy heatmap diagram, where the color code shows a lower Rényi entropy dip right before the periodic collisions of the kinks.

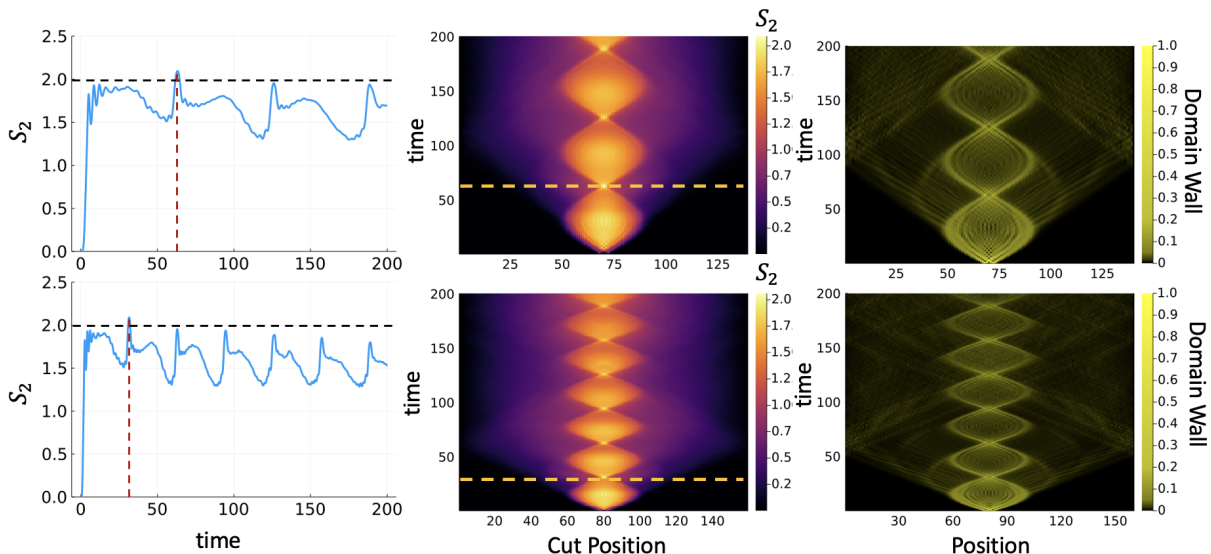


FIG. 12. The half-chain Rényi entropy S_2 (left), the Rényi entropy map with different bipartite cut (middle), and the domain wall profile across link positions (right) for $g = -J = 0.25, h = 0.05, L = 140$ (top) and $g = -J = 0.5, h = 0.1, L = 160$ (bottom).

Appendix D: MPS Implementation and Computational Complexity

Many 1D systems can be analyzed efficiently using matrix product states (MPS). Previous work has explored entanglement asymmetry in the context of exact diagonalization [39], where large system sizes can only be explored for non-interacting models, and iTEBD time evolution for interacting models with integrability [63]. Another recent work [64] has explored entanglement asymmetry in matrix product states in the context of the ground state of a symmetric Hamiltonian undergoing spontaneous symmetry breaking. Here we implement the computation of the ΔS_2 entanglement asymmetry given an MPS for generic models that includes non-integrability, an interacting Hamiltonian, and a more general setting that includes non-local entanglement asymmetry.

We will now outline the general algorithm for the straightforward computation of the bipartite entanglement asymmetry for MPS.

1. Perform the time evolution of the MPS from $|\psi(t - \Delta t)\rangle$ to $|\psi(t)\rangle$ with the choice of tMPS, tDMRG or TEBD.
2. Choose the orthogonality center of the MPS across which the bipartite 2nd Rényi entropy $S_2(\rho_A)$ is calculated (mixed canonical MPS).
3. Contract the indices efficiently (with increasing bond dimensions) from one end of the MPS to the orthogonality center to construct the reduced density matrix ρ_A (Fig. 13(a)).
4. With ρ_A , split the numerical integration of Eq. (15) into $k + 1$ steps. For each discrete λ perform the MPO application onto the ρ_A [Fig. 13(b) or (c)]. Perform the full trace after evaluating $e^{i\lambda Q} \rho_A e^{-i\lambda Q} \rho_A$. The MPO application and tracing is done $k + 1$ times to evaluate $S_2(\rho_{A,Q})$ and subsequently ΔS_2 .

In this work, we calculate two different types of entanglement asymmetry: onsite entanglement asymmetry (such as the magnetization entanglement asymmetry previous considered in [39] with $Q_A = \sum_{i=2}^l \sigma_i^z$) and link-type entanglement asymmetry (in our case, the kink entanglement asymmetry with $Q_A = \sum_{i=1}^{l-1} \sigma_i^z \sigma_{i+1}^z$, shown in Fig. 13(c)).

We will comment on the computational complexity of our algorithm above, and possible speed up that could possibly be implemented in a future work. In iTensor, working with density matrices is actually sub-optimal since it creates MPO with bond dimension D^2 , which we illustrate in Fig. 14. Depending on the details of how iTensor package handles the contraction of two (different) reduced density matrices, this computation can either scale as $\mathcal{O}(Ld^3D^8)$ in the worst case or $\mathcal{O}(Ld^3D^6)$ in the most optimal case. Dealing with reduced density matrices directly is more straightforward in code development with existing methods in iTensor, but severely limits the simulability of Rényi

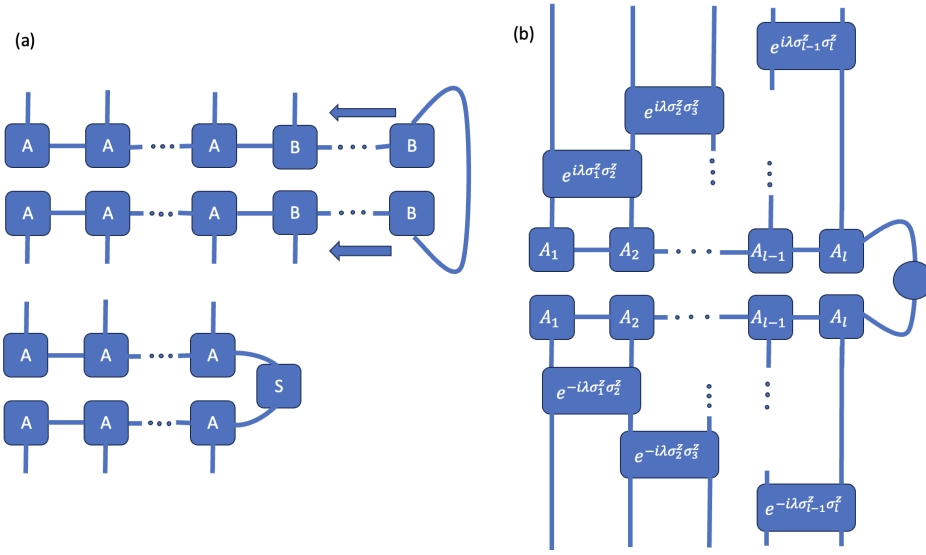


FIG. 13. (a) The order of contraction of the legs of the tensor of the MPS wave function in the construction of the reduced density matrix $\rho_A = \text{Tr}_B(|\psi_{MPS}\rangle\langle\psi_{MPS}|)$ is shown in the arrow. (b) The MPO operators $e^{\pm i\lambda Q} = \prod_{i=1}^l e^{\pm i\lambda\sigma_i^z}$ (in site-type symmetry resolved entropy), and (c) The MPO operators $e^{\pm i\lambda Q} = \prod_{i=1}^{l-1} e^{\pm i\lambda\sigma_i^z\sigma_{i+1}^z}$ (in link-type symmetry resolved entropy) are applied successively via the DMRG algorithm. If the integral is split into $k+1$ steps, λ takes discrete values in the interval $[-2\pi, 2\pi]$ and this calculation is done for $(k+1)$ different λ before the Trapezoid Rule is applied to obtain $\rho_{A,Q}$

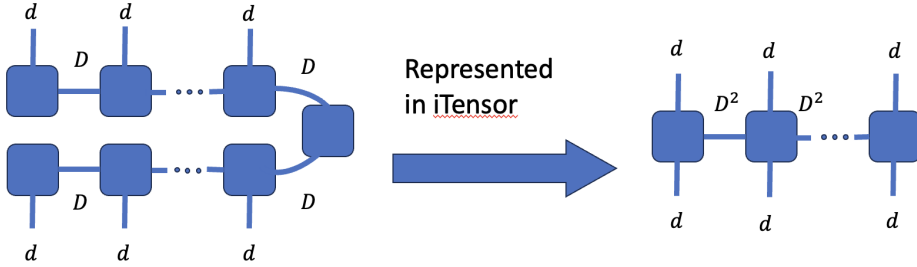


FIG. 14. In iTensor, taking an outer product of an MPS $|\psi\rangle$ with itself (with bond dimension D) automatically forms an MPO density matrix with bond dimensions D^2 .

entropy evolution to later times when bond dimension is large everywhere on the spin chain. This is the case for string breaking (kink number violating, generic case) situation when $g \neq -J$, as shown in Fig. 6 when we attempt to calculate Rényi asymmetry directly with density matrix contractions and issue with computational cost only allows time evolution for early times ($t = 10$).

Instead, an optimal approach is shown in Fig. 15. The algorithm represented pictorially in Fig. 15 will necessitate contractions without constructing reduced density matrices directly. In this approach, we contract tensors individually and avoid the dealing with the full D^2 bond dimensions of each ρ_A MPO link. The algorithm in this case will dramatically improve the complexity to $\mathcal{O}(LdD^3)$, but it comes with a more complicated code development. We will leave the development of a more efficient entanglement asymmetry computation as a future research avenue.

Appendix E: Kramers-Wannier Unitary Transformation and the XY Model

Given the problem that the kink entanglement asymmetry at the interface cannot be tracked in our current basis, we perform a site-to-link transformation to map link variables (such as the domain wall operator $\sigma_i^z\sigma_{i+1}^z$) to site variable. This has traditionally been associated to the Kramers-Wannier duality on a 2D Ising Model. In the context of the (1+1)D Transverse Field Ising Model, one cannot construct a unitary that represents the Kramers-Wannier duality

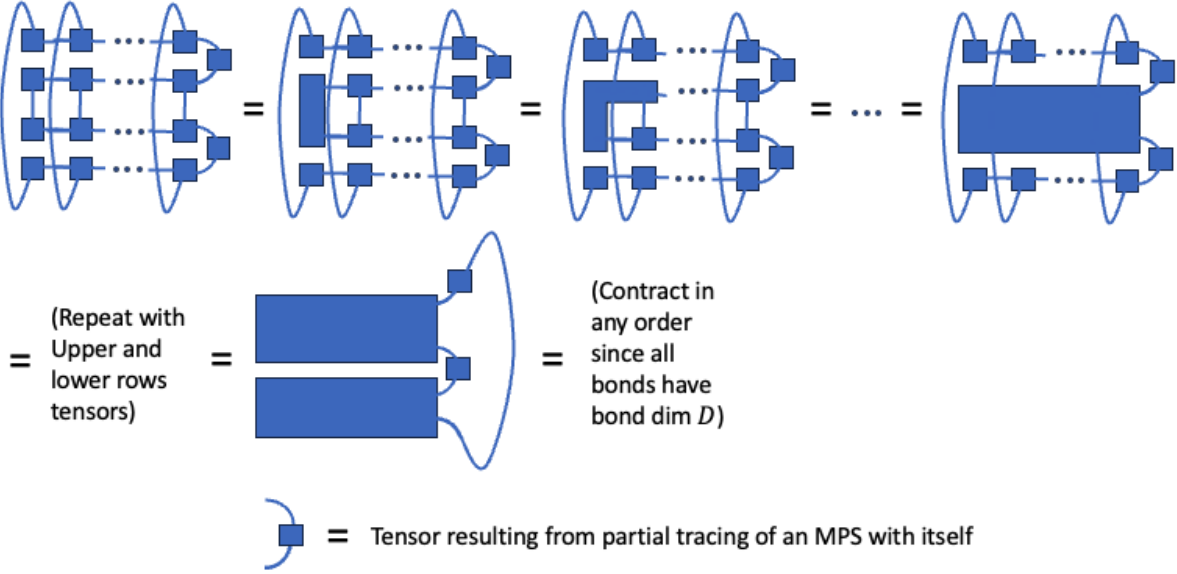


FIG. 15. Minimal contraction order for individual tensors to compute $\text{Tr}(e^{i\lambda Q} \rho_A e^{-i\lambda Q} \rho_A)$. Here the top 2 and bottom 2 rows of tensors can come from different reduced density matrix. The strategy for implementation here is to perform contractions of individual tensor component in MPS wave functions without first forming the density matrix MPOs, and the size tensor from partial trace can also be formed partial inner product of MPS wave function with itself.

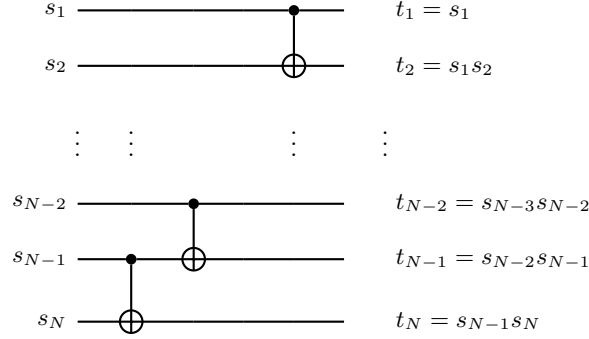


FIG. 16. This quantum circuit implements the Kramers-Wannier Unitary on an open Ising spin chain.

since it maps the ferromagnetic phase of the Transverse Field Ising model ($g < 1$) with ground state degeneracy and spin-flip symmetry breaking to the paramagnetic phase of the Transverse Field Ising Model ($g > 1$) with non-degenerate ground state possessing spin-flip symmetry. Hence, we wish to clarify from the onset that our unitary defined below is a Kramers-Wannier unitary transformation that is only well-defined on an open chain and serves to perform a basis transformation.

We define a Kramers-Wannier unitary U_{KW} that is distinct from the Kramers-Wannier duality in the sense that: (1) it is defined on open boundary condition, (2) it maps all links to sites except the first site, which also maps to the first site in the 'dual' lattice, and (3) the unitary is not self-dual, i.e., $U_{KW}^2 \neq I$. In this way the dimension of the Hilbert space is preserved, since an open chain with N sites only has $N - 1$ links. The unitary is defined and represented in the quantum circuit language as a series of CNOT gates, as shown in Fig. 16.

Here, we have defined $|0\rangle \equiv |\uparrow\rangle \equiv |s = +1\rangle$, $|1\rangle \equiv |\downarrow\rangle \equiv |s = -1\rangle$, and one can verify that the action of the CNOT gate on the target qubit/spin matches the value of the product of spin $t_j = s_{j-1}s_j$. In this dual lattice picture, we can perform the unitary transformation on the Hamiltonian $H' = U_{KW} H U_{KW}^\dagger$ to get, in this dual picture,

$$H' = - \left[J_0 \sum_{i=2}^L \sigma_i^z + g \sum_{i=2}^{L-1} \sigma_i^x \sigma_{i+1}^x + h \sum_{i=1}^L \left(\prod_{j=1}^i \sigma_j^z \right) - J \sum_{i=2}^{L-1} \sigma_i^y \sigma_{i+1}^y \right], \quad (\text{E1})$$

where the Kramers-Wannier unitary U_{KW} maps $\sigma_i^z \rightarrow \prod_{j=1}^i \sigma_j^z$, $\sigma_i^x \rightarrow \sigma_i^x \sigma_{i+1}^x$, and the coefficients above identify the origin of the terms of the original Hamiltonian in Eq. (1). While the form of the Kramers-Wannier mapping for σ_i^z and σ_i^x has been given in [65], to our knowledge the explicit form of the unitary has not been given in earlier works. In this dual picture, the symmetry operator is transformed as $\prod_{i=1}^{L-1} e^{\pm i\lambda \sigma_i^z \sigma_{i+1}^z} \rightarrow \prod_{i=2}^L e^{\pm i\lambda \sigma_i^z}$, the total magnetization of the left half of the spin chain except the magnetization on site 1.

Interestingly, while the original Hamiltonian had 4 sectors associated with local boundary spins σ_1^z and σ_L^z , our transformed Hamiltonian now commutes with σ_1^z as well as with the parity operator $\prod_{i=1}^L \sigma_i^z$ which is non-local. We also note that the original Hamiltonian preserves the parity of the kink number, even when $g \neq -J$. This form also makes explicit the conservation of kink parity, where kink is now represented by the number of down spins.

When $h=0$ in the Hamiltonian Eq. (E1), this Hamiltonian is the XY model. This can readily be cast into the free fermion picture using the Jordan Wigner Transformation, with the resulting Hamiltonian (ignoring constant terms)

$$H = - \left[2J_0 \sum_{j=2}^L c_j^\dagger c_j + (g+J) \sum_{j=2}^{L-1} (c_j^\dagger c_{j+1}^\dagger + c_{j+1} c_j) + (g-J) \sum_{j=2}^{L-1} (c_j^\dagger c_{j+1} + c_{j+1}^\dagger c_j) \right]. \quad (\text{E2})$$

In this form, the fermions represent the domain walls, and we can read off that the hopping strength of the domain wall is $(g-J)$ while the kink number violation term comes with the strength $(g+J)$.

Appendix F: Upper bound on Rényi Entropy for $h=0$ and kink-number preservation.

In this appendix, we prove that starting with a domain wall, and evolving with our Hamiltonian with $J = -g$ and $h = 0$ the second order half chain Rényi entropy $S_2 = -\log_2(\text{Tr}(\rho_A^2))$ is bound by 2 at all times. Concretely, we consider an initial state of the form:

$$|\psi(0)\rangle = |\uparrow \dots \uparrow \downarrow_x \dots \downarrow_{y-1} \uparrow_y \dots \uparrow\rangle \quad (\text{F1})$$

To compute the evolution, we first apply the Kramers-Wannier U_{KW} , mapping the state to:

$$U_{KW}|\psi(0)\rangle = |1\dots(-1)_x 111(-1)_y 11 \dots 1\rangle. \quad (\text{F2})$$

Via a Jordan Wigner transformation this state will become the two particle state

$$U_{KW}|\psi(0)\rangle = c_x^\dagger c_y^\dagger |\text{vac}\rangle. \quad (\text{F3})$$

As explained above, the evolution of the state in the Jordan-Wigner picture is governed by the quadratic fermion Hamiltonian (E2). In particular, when $g = -J$, the Hamiltonian does not involve pair creation terms. Under such evolution, the creation operators in (F3) transform as:

$$c_\alpha^\dagger \longrightarrow \sum_j u_{\alpha j} c_j^\dagger \quad (\text{F4})$$

with a unitary $L \times L$ matrix u . Therefore the evolved state is of the form:

$$U_{KW}|\psi(t)\rangle = \sum_{i,j} u_{xi} u_{yj} c_i^\dagger c_j^\dagger |\text{vac}\rangle = \sum_{i<j} (u_{xi} u_{yj} - u_{xj} u_{yi}) c_i^\dagger c_j^\dagger |\text{vac}\rangle \quad (\text{F5})$$

We now undo the Kramers-Wannier transformation to get:

$$|\psi(t)\rangle = \sum_{i<j} (u_{xi} u_{yj} - u_{xj} u_{yi}) |\uparrow \dots \uparrow \downarrow_i \dots \downarrow_{j-1} \uparrow_j \dots \uparrow\rangle \quad (\text{F6})$$

We now proceed by bounding the Schmidt rank of the state (F6). We expand the summation explicitly as:

$$\begin{aligned} |\psi(t)\rangle &= \sum_{i \leq L_A} \sum_{j > L_A} (u_{xi} u_{yj} - u_{xj} u_{yi}) |\uparrow \dots \uparrow \downarrow_i \dots \downarrow_{j-1} \uparrow_j \dots \uparrow_N\rangle \\ &+ \sum_{i > L_A} \sum_{j > i} (u_{xi} u_{yj} - u_{xj} u_{yi}) |\uparrow \dots \uparrow \downarrow_i \dots \downarrow_{j-1} \uparrow_j \dots \uparrow_N\rangle \\ &+ \sum_{i < j} \sum_{j \leq L_A} (u_{xi} u_{yj} - u_{xj} u_{yi}) |\uparrow \dots \uparrow \downarrow_i \dots \downarrow_{j-1} \uparrow_j \dots \uparrow_N\rangle \\ &= (\sum_{i \leq L_A} u_{xi} |\uparrow \dots \uparrow \downarrow_i \dots \downarrow_{L_A}\rangle) \otimes (\sum_{j > L_A} u_{yj} |\downarrow_{L_A+1} \dots \downarrow_{j-1} \uparrow_j \dots \uparrow_N\rangle) \\ &- (\sum_{i \leq L_A} u_{xj} |\uparrow \dots \uparrow \downarrow_i \dots \downarrow_{L_A}\rangle) \otimes (\sum_{j > L_A} u_{yi} |\downarrow_{L_A+1} \dots \downarrow_{j-1} \uparrow_j \dots \uparrow_N\rangle) \\ &+ |\uparrow \dots \uparrow \uparrow_{L_A}\rangle \otimes (\sum_{i > L_A} \sum_{j > i} (u_{xi} u_{yj} - u_{xj} u_{yi}) |\uparrow \dots \uparrow \downarrow_i \dots \downarrow_{j-1} \uparrow_j \dots \uparrow_N\rangle) \\ &+ (\sum_{i < j} \sum_{j \leq L_A} (u_{xi} u_{yj} - u_{xj} u_{yi}) |\uparrow \dots \uparrow \downarrow_i \dots \downarrow_{j-1} \uparrow_j \dots \uparrow_{L_A}\rangle) \otimes |\uparrow \dots \uparrow \uparrow_N\rangle. \end{aligned} \quad (\text{F7})$$

Observe that in the last line we have explicitly separated $|\psi(t)\rangle$ into a combination of the form:

$$|\psi(t)\rangle = \sum_{\alpha=1}^4 |\phi_{\alpha}\rangle \otimes |\tilde{\phi}_{\alpha}\rangle. \quad (\text{F8})$$

Note that for the rest of the argument, it doesn't matter if $\phi_{\alpha}, \tilde{\phi}_{\alpha}$, are normalized or represent orthogonal sets. Indeed, the form (F8) immediately implies that the Schmidt rank of the state $|\psi(t)\rangle$ with respect to this partition is at most $\text{Sch}(\psi(t)) \leq 4$ (see Problem 2.2 in [66]). Since the logarithm of the Schmidt number is a bound on entropy (Von Neumann entropy, and as consequence also Rényi entropy) we have that:

$$S_2 \leq \log_2 \text{Sch}(\psi(t)) \leq \log_2 4 = 2. \quad (\text{F9})$$